



1 Improving the Retrieval of XCO₂ from Total Carbon Column 2 Network Solar Spectra

3 Authors: Joseph Mendonca¹, Kimberly Strong¹, Debra Wunch¹, Geoffrey C. Toon², David A.
 4 Long³, Joseph T. Hodges³, Vincent T. Sironneau³, and Jonathan E. Franklin⁴.

5 1. Department of Physics, University of Toronto, Toronto, ON, Canada

6 2. Jet Propulsion Laboratory, Pasadena, CA, USA

7 3. National Institute of Standards and Technology, Gaithersburg, MD, USA

8 4. Harvard John A. Paulson School of Engineering and Applied Sciences, Cambridge, MA, USA

9 *Correspondence to:* Joseph Mendonca (joseph.mendonca@utoronto.ca)

10 **Abstract.** High-resolution absorption spectra of the $a^1\Delta_g \leftarrow X^3\Sigma_g^-$ O₂ band measured using cavity ring-down
 11 spectroscopy were fitted using the Voigt and speed-dependent Voigt line shapes. We found that the speed-dependent
 12 Voigt line shape was better able to model the measured absorption coefficients than the Voigt line shape. Total
 13 columns of O₂ were retrieved from ground-based high-resolution absorption spectra from four Total Carbon Column
 14 Observing Network (TCCON) sites using both Voigt and speed-dependent Voigt line shapes to calculate absorption
 15 coefficients. A lower O₂ concentration was retrieved with the speed-dependent Voigt line shape, with the difference
 16 increasing as a function of solar zenith angle. CO₂ total columns were also retrieved from the same spectra using a
 17 Voigt line shape and speed-dependent Voigt with line mixing. The column-averaged dry-air mole fraction of CO₂
 18 (XCO₂) was calculated using the CO₂ and O₂ columns retrieved with both line shapes from measurements made
 19 over a one-year period at the four sites and compared. The inclusion of speed dependence reduces the airmass
 20 dependence of XCO₂. The TCCON empirical airmass correction factor for XCO₂ derived from a year of
 21 measurements from TCCON sites at Darwin, Lamont, and Park Falls for XCO₂ improved from -0.0071 ± 0.0057 to $-$
 22 0.0012 ± 0.0054 when speed dependence was included. XCO₂ retrieved with the Voigt and speed-dependent Voigt
 23 line shapes was compared to aircraft profiles measured at 13 TCCON sites. The bias between the TCCON
 24 measurements and the integrated aircraft profile measurements was reduced from 0.9897 ± 0.0005 to 1.0041 ± 0.0005
 25 for XCO₂ retrieved with the Voigt and speed-dependent Voigt line shapes respectively. These results suggest that
 26 speed dependence should be included in the forward model when fitting near-infrared CO₂ and O₂ spectra to
 27 improve the accuracy of XCO₂ measurements.

28 1. Introduction

29 Accurate remote sensing of greenhouse gases (GHGs), such as CO₂, in Earth's atmosphere is important for studying
 30 the carbon cycle in order to better understand and predict climate change. The absorption of solar radiation by O₂ in
 31 the Earth's atmosphere is important because it can be used to study the properties of clouds and aerosols, and to
 32 determine vertical profiles of temperature and surface pressure. Mlawer et al. (1998) recorded solar absorption
 33 spectra in the near-infrared (NIR) region to study the $a^1\Delta_g \leftarrow X^3\Sigma_g^-$ band of O₂ centered at 1.27 μm (which will be



referred to as the 1.27 μm band). The spectra were compared to a line-by-line radiative transfer model and the differences between the measured and calculated spectra showed the need for better absorption coefficients in order to accurately model the 1.27 μm band (Mlawer et al., 1998). Subsequently, spectroscopic parameters needed to calculate the absorption coefficients from discrete transitions of the 1.27 μm band were measured in multiple studies (Cheah et al., 2000; Newman et al., 1999, 2000; Smith and Newnham, 2000), as was collision-induced absorption (CIA) (Maté et al., 1999; Smith and Newnham, 2000), while Smith et al. (2001) validated the work done in Smith and Newnham (2000) using solar absorption spectra.

The 1.27 μm band is of particular importance to the Total Carbon Column Observing Network (TCCON) (Wunch et al., 2011). TCCON is a ground-based remote sensing network that makes accurate and precise measurements of GHGs for satellite validation and carbon cycle studies. Using the O_2 column retrieved from solar absorption spectra, the column-averaged dry-air mole fraction of CO_2 ($X\text{CO}_2$) has been shown to provide better precision than using the surface pressure to calculate $X\text{CO}_2$ (Washenfeller et al., 2006). The O_2 column is retrieved from the 1.27 μm band because of its close proximity to the spectral lines used to retrieve CO_2 , thereby reducing the impact of solar tracker mis-pointing and an imperfect instrument line shape (ILS) (Washenfeller et al., 2006). To improve the retrievals of O_2 from the 1.27 μm band, Washenfeller et al. (2006) found that adjusting the spectroscopic parameters in HITRAN 2004 (Rothman et al., 2005) decreased the airmass and temperature dependence of the O_2 column. These revised spectroscopic parameters were included in HITRAN 2008 (Rothman et al., 2009). Atmospheric solar absorption measurements from this band made at the Park Falls TCCON site by Washenfeller et al. (2006) were the first measurements to observe the electric-quadrupole transitions (Gordon et al., 2010). Leshchishina et al. (2011, 2010) subsequently used cavity-ring-down spectra to retrieve spectroscopic parameters for the 1.27 μm band using a Voigt spectral line shape and these parameters were included in HITRAN 2012 (Rothman et al., 2013).

Extensive spectral line shape studies have been performed for the O_2 A-band, which is centered at 762 nm and used by the Greenhouse Gases observing Satellite (GOSAT) (Yokota et al., 2009) and the Orbiting Carbon Observing (OCO-2) satellite (Crisp et al., 2004) to determine surface pressure. These studies showed that the Voigt line shape was inadequate to describe the spectral line shape of discrete O_2 lines in the A-Band; the need to take into account Dicke narrowing was shown in (Long et al., 2010; Predoi-Cross et al., 2008) and line mixing in (Predoi-Cross et al., 2008; Tran et al., 2006; Tran and Hartmann, 2008). Tran and Hartmann (2008) showed that including line mixing when calculating the O_2 A-band absorption coefficients reduced the airmass dependence of the O_2 column retrieved from TCCON spectra.

The need to include non-Voigt effects when calculating absorption coefficients for the O_2 1.27 μm band was first shown in Hartmann et al. (2013) and Lamouroux et al. (2014). In Hartmann et al. (2013) and Lamouroux et al. (2014), Lorentzian widths were calculated using the re-quantized classical molecular-dynamics simulations (rCMDs) and used to fit cavity-ring-down spectra with a Voigt line shape for some isolated transitions in the O_2 1.27 μm band. The studies concluded that a Voigt line shape is insufficient for modeling the spectral lines of the O_2 1.27 μm band and that effects such as speed dependence and Dicke narrowing should be included in the line shape calculation.



In this study, air-broadened cavity-ring-down spectra of the O₂ 1.27 μm band were fitted using a spectral line shape that takes into account speed dependence. The corresponding spectroscopic parameters for the speed-dependent Voigt line shape were used to calculate absorption coefficients when fitting high-resolution solar absorption spectra. These new O₂ columns were combined with CO₂ columns from Mendonca et al. (2016) to calculate XCO₂ and compared with XCO₂ retrieved using a Voigt line shape. Section 2 details the formulas used to calculate absorption coefficients using different spectral line shapes. In Section 3, we describe the retrieval of spectroscopic parameters from three air-broadened cavity-ring-down spectra fitted with a speed-dependent Voigt line shape. For Section 4, the speed-dependent line shape along with the retrieved spectroscopic parameters is used to fit solar absorption spectra from four TCCON sites and retrieve total columns of O₂, which is compared to O₂ retrieved using a Voigt line shape. In Section 5, we investigate the change in the airmass dependence of XCO₂ with the new O₂ parameters. In Section 6, we discuss our results and their implications for remote sensing of greenhouse gases.

2. Absorption Coefficient Calculations

2.1 Voigt Line Shape

The Voigt line shape is the convolution of the Lorentz and the Doppler line shapes. The corresponding absorption coefficient, k , at a given wavenumber ν becomes :

$$k(\nu) = N \sum_j S_j \left(\frac{1}{\gamma_{Dj}} \right) \left(\frac{\ln(2)}{\pi} \right)^{1/2} \text{Re}[c(\nu, x_j, y_j)] \quad (1)$$

where N is the number density, S_j is the line intensity of spectral line j , γ_{Dj} is the Doppler half-width (HWHM), c is the complex error function, and

$$x_j = \frac{(\nu - \nu_j^0 - P\delta_j^0)}{\gamma_{Dj}} (\ln(2))^{1/2}, \quad y_j = \frac{\gamma_{Lj}}{\gamma_{Dj}} (\ln(2))^{1/2}. \quad (2)$$

Here, ν_j^0 is the position of the spectral line j , P is the pressure, and δ_j^0 is the pressure-shift coefficient. The Lorentz half-width, γ_{Lj} , is calculated using:

$$\gamma_{Lj}(T) = P \gamma_{Lj}^0 \left(\frac{296}{T} \right)^n \quad (3)$$

where γ_{Lj}^0 is the air-broadened Lorentz half-width coefficient (at reference temperature 296 K) and n is the exponent of temperature dependence.

2.2 Speed-Dependent Voigt Line Shape

To take speed dependence into account, we use the speed-dependent Voigt line shape (Ciuryło, 1998) with the quadratic representation of the Lorentz width and pressure shift (Rohart et al., 1994):



$$k(v) = N \left(\frac{2}{\pi^{1/2}} \right) \sum_j S_j \int_{-\infty}^{\infty} e^{-v^2} V \left(\tan^{-1} \left[\frac{x_j - B a_{\delta_j} ((V)^2 - 1.5) + V}{y_j (1 + a_{\gamma_{L_j}} ((V)^2 - 1.5))} \right] \right) dV \quad (4)$$

94 where $a_{\gamma_{L_j}}$ is the speed-dependent Lorentz width parameter (unitless) for line j , a_{δ_j} is the speed- dependent pressure-
 95 shift parameter (unitless), B is $\frac{(\ln(2))^{1/2}}{\gamma_{D_j}}$, V is the ratio of the absorbing molecule's speed to the most probable speed
 96 of the absorbing molecule, and all other variables are defined before.

97 3. Fitting Laboratory Spectra

98 O₂, unlike CO₂ and CH₄, cannot produce an electric dipole moment and therefore should not be infrared active.
 99 However, O₂ has two unpaired electrons in the ground state that produce a magnetic dipole moment. Due to the
 100 unpaired electrons in the ground state ($X^3\Sigma_g^-$) the rotational state (N) is split into three components which are given
 101 by $J = N-1$, $J = N$, and $J = N+1$, while in the upper state ($a^1\Delta_g$), $J = N$. When labeling a transition, the following
 102 nomenclature is used $\Delta N(N'')\Delta J(J'')$ (Leshchishina et al., 2010), where ΔN is the difference between N' in the upper
 103 state and N'' in the lower state, ΔJ is the difference between J' in the upper state and J'' in the lower state. The
 104 magnetic transitions of $a^1\Delta_g \leftarrow X^3\Sigma_g^-$ allow for $\Delta J=0, \pm 1$. This leads to 9 branches observed: $P(N'')Q(J'')$,
 105 $R(N'')Q(J'')$, and $Q(N'')Q(J'')$, for $\Delta J=0$, $O(N'')P(J'')$, $P(N'')P(J'')$, and $Q(N'')P(J'')$, for $\Delta J=-1$, and $S(N'')R(J'')$,
 106 $R(N'')R(J'')$, and $Q(N'')R(J'')$, for $\Delta J=1$.

107 Absorption coefficients for three room temperature air-broadened (NIST Standard reference material® 2659a
 108 containing 79.28 % N₂, 20.720(43) % O₂, 0.0029 % Ar, 0.00015 % H₂O, and 0.001 % other compounds) spectra
 109 were measured at the National Institute of Standards and Technology (NIST) using the frequency-stabilized cavity-
 110 ring-down spectroscopy (FS-CRDS) technique (Hodges et al., 2004; Hodges, 2005). The absorption spectra were
 111 acquired at pressures of 131 kPa, 99.3 kPa, and 66.9 kPa, at temperatures of 296.28 K, 296.34 K, and 296.30 K
 112 respectively. Figure 1a shows the three measured absorption spectra. A more detailed discussion of the present FS-
 113 CRDS spectrometer can be found in Lin et al. (2015).

114 The spectra were fitted individually using a Voigt line shape (Eq. 1), with S_j , $\gamma_{L_j}^o$, and δ_j^o for the main isotope of the
 115 magnetic dipole lines of the O₂ 1.27 μm band for lines with an intensity greater than $7.0 \times 10^{-28} \text{ cm}^{-1}/(\text{molecule cm}^{-2})$.
 116 The spectroscopic parameters measured in Leshchishina et al. (2011) for the spectral lines of interest were used as
 117 the a priori for the retrieved spectroscopic parameters. The line positions were left fixed to the values measured in
 118 Leshchishina et al. (2011), and all other O₂ spectral lines (intensity less $7.0 \times 10^{-28} \text{ cm}^{-1}/(\text{molecule cm}^{-2})$) were
 119 calculated using a Voigt line shape with spectroscopic parameters from HITRAN 2012 (Rothman et al., 2013).
 120 Spectral fits were done using the lsqnonlin function in Matlab, with a user-defined Jacobian matrix. The Jacobian
 121 was constructed by taking the derivative of the absorption coefficients with respect to the parameters of interest.
 122 Using an analytical Jacobian instead of the finite difference method is both computationally faster and more
 123 accurate. The Voigt line shape was calculated using the Matlab code created by Abrarov and Quine (2011) to
 124 calculate the complex error function and its derivatives. To take collision-induced absorption (CIA) into account, a



125 set of 50 Legendre polynomials were added together by retrieving the weighting coefficients needed to add the
 126 polynomials to fit the CIA for each spectrum. Figure 1b shows the residual (measured minus calculated absorption
 127 coefficients) when using a Voigt line shape with the retrieved spectroscopic parameters. The plot shows that residual
 128 structure still remains for all three spectra. The Root Mean Square (RMS) residual values for the spectra are given
 129 by the legend at the side of the plot.

130 Figure 2 is the same plot as Figure 1 but for the P(11)P(11), P(11)Q(10), P(9)P(9), and P(9)Q(8) spectral lines only.
 131 Figure 2b shows that for all four spectral lines there is a “W” shaped residual at the line center. The P(11)P(11) line
 132 was also measured by Hartmann et al. (2013) at pressures ranging from 6.7 to 107 kPa. Figure 5 of Hartmann et al.
 133 (2013) shows the P(11)P(11) line at a pressure of 66.7 kPa, which is approximately the pressure of the 66.9 kPa
 134 spectrum (blue spectrum in Figure 1 and 2). When one compares the blue residual of the P(11)P(11) line in Figure
 135 2b to that of the residual of the left panel of Figure 5 of Hartmann et al. (2013), one can see that the residuals are the
 136 same. Figure 6 of Hartmann et al. (2013) show that the amplitude of the residual increases with decreasing pressure,
 137 which is also seen in Figure 2b. Figure 3 of Lamouroux et al. (2014) shows the same “W” residual for the P(9)P(9)
 138 lines and that the amplitude of the residual increases with decreasing pressure (although for lower pressures)
 139 consistent with the results for the P(9)P(9) line in Figure 2b.

140 Figure 1c shows the residual when using the speed-dependent Voigt (Eq. 4) to fit each spectrum individually. To use
 141 Eq. (4) requires integration over all possible speeds, which is not computationally practical, so we employ the
 142 simple numerical integration scheme as was done by Wehr (2005). When fitting the spectra, parameters S_j , $\gamma_{L_j}^o$, δ_j^o ,
 143 $a_{\gamma_{L_i}}$ and a_{δ_j} were retrieved for lines of intensity greater than $7.0 \times 10^{-28} \text{ cm}^{-1}/(\text{molecule cm}^{-2})$, while all other O₂ lines
 144 were calculated using a Voigt line shape and spectroscopic parameters from HITRAN 2012 (Rothman et al., 2013b).
 145 The Jacobian matrix was created by taking the derivative with respect to each parameter of interest, as was done
 146 with the Voigt fits. By taking speed-dependent effects into account, the residuals were reduced to 25 times smaller
 147 than those for the Voigt fit and the RMS residuals (given in the legend of Figure 1c) are 10 times smaller. However,
 148 some residual structure still remains, which is more evident in the in the Q and R branches than the P branch. Figure
 149 2c shows the four lines in the P branch, as discussed when analyzing the Voigt fits. A small residual “W” remains at
 150 line center, as well as residuals from weak O₂ lines.

151 Figure 3 shows the averaged intensity, Lorentz width coefficient, pressure shift coefficient, and speed-dependent
 152 shift coefficient, retrieved from the three spectra, plotted as a function of J'' . The intensity, Lorentz widths, and
 153 pressure shifts show a J'' dependence for these parameters for the P and R sub-branches. The measured Lorentz
 154 widths and pressure shifts for the Q sub-branches show a J'' dependence but are not as strong as the P and R sub-
 155 branches. This is because the Q branch lines are broadened enough to blend with each other since they are spaced
 156 closer together than the P or R branch lines. Figure 1c shows that some of the residual structure in the Q branch
 157 increases with pressure and is partly due to the blending of these transitions as the pressure increases. The weak O₂
 158 absorption lines also blend in with the Q branch, contributing to the residual structure in Figure 1c. We tried
 159 retrieving the spectroscopic parameters for the weak O₂ absorption lines, but since they were overlapping with the



strong O₂ lines, it was not possible. Figure 4a shows the retrieved speed-dependent width averaged over the three spectra, plotted as a function of J'' , showing that it increases with J'' . Error bars correspond to the 2σ standard deviation and are large regardless of sub-branch. Figure 4b shows the retrieved speed-dependent width for the PQ sub-branch for the different pressures. The speed-dependent width shows the same J'' dependence regardless of pressure, but also increases with decreasing pressure as is the case for sub-branches. It should be noted that the speed-dependent width parameter should be independent of pressure.

4. Fitting Solar Spectra

High-resolution solar absorption spectra were measured at four TCCON sites using a Bruker IFS 125HR FTIR spectrometer with a room temperature InGaAs detector at a spectral resolution of 0.02 cm⁻¹ (45 cm maximum optical path difference). The raw interferograms recorded by the instrument were processed using the I2S software package (Wunch, D. et al., 2015) that corrects them for solar intensity variations (Keppel-Aleks et al., 2007), phase errors (Mertz, 1967), and laser sampling errors (Wunch, D. et al., 2015), and then fast Fourier transforms the interferograms into spectra (Bergland, 1969). The GGG software package (Wunch, D. et al., 2015) is used to retrieve total columns of atmospheric trace gases. GFIT is the main code that contains the forward model, which calculates a solar absorption spectrum using a line-by-line radiative transfer model and an iterative non-linear least square fitting algorithm that scales an a priori gas profile to obtain the best fit to the measured spectrum. A priori profiles for GHGs are created by an empirical model in GGG that is based on measurements from the balloon-borne JPL MkIV Fourier Transform Spectrometer (FTS) (Toon, 1991), the Atmospheric Chemistry Experiment (ACE) FTS instrument aboard SCISAT (Bernath et al., 2005), and in situ GLOBALVIEW data (Wunch et al., 2011). Temperature and pressure profiles, as well as H₂O a priori profiles are generated from the National Centers for Environmental Prediction (NCEP) data. The calculations are performed for 71 atmospheric layers (0 km to 70 km), so all a priori profiles are generated on a vertical grid of 1 km.

In the current GGG software package (Wunch, D. et al., 2015), the forward model of GFIT calculates absorption coefficients for the discrete lines of the O₂ 1.27 μm band using a Voigt line shape and spectroscopic parameters from Washenfelder et al. (2006a) and Gordon et al. (2010). To take CIA into account, absorption coefficients are calculated using a Voigt line shape and spectroscopic parameters from the foreign-collision-induced absorption (FCIA) and self-collision-induced absorption (SCIA) spectral line lists provided with the GGG software package (Wunch, D. et al., 2015). Spectroscopic parameters in the FCIA and SCIA line lists were retrieved by Geoff Toon by fitting the laboratory spectra of Smith and Newnham (2000). This was done by retrieving the integrated absorption at every 1 cm⁻¹ of the spectrum and using a Voigt line shape, with fixed Lorentz width and no pressure shift. In GFIT, a volume scale factor is retrieved for the CIA and discrete lines separately so that the O₂ column is derived from the discrete lines of the 1.27 μm band only. The continuum level and tilt of the 100% transmission level is fitted using a weighted combination of the first two Legendre polynomials. Absorption coefficient for all other trace gases are calculated using a Voigt line shape and spectroscopic parameters from the atm.101 line list (Wunch, D. et al., 2015) and solar lines are fitted using the solar line list (Wunch, D. et al., 2015).



Figure 5 shows the spectral fit to a solar absorption spectrum recorded at Eureka on March 27, 2015, at a solar zenith angle (SZA) of 81.32° (airmass of 6.3). This spectrum is an average of 5 Eureka scans. The TCCON standard is single scan but 5 scans were averaged to decrease the noise. The measured spectrum (red circles), calculated spectrum (black circles) and transitions from all gases in the window (colored lines, refer to the legend for different gases) are shown in Figure 5b. The residual obtained using a Voigt line shape to calculate the discrete lines of the O_2 $1.27\ \mu\text{m}$ band is shown in red in Figure 5a. The blue residual is the result of using a speed-dependent Voigt line shape with the spectroscopic parameters retrieved from fitting the absorption coefficients in Section 3. To decrease the amount of time it takes to calculate the absorption coefficients, the quadratic-Speed Dependent Voigt (qSDV) computational approach of Ngo et al. (2013) and Tran et al. (2013) was used instead of Eq. (4) since it requires the Voigt calculation only twice, while Eq. (4) requires numerical integration scheme with 33 iterations. The temperature-dependent parameter of the Lorentz width of the discrete lines of the O_2 $1.27\ \mu\text{m}$ band reported in HITRAN 2012 was used to take temperature dependence into account for $\gamma_{L_j}(T)$. There was only a slight improvement in the fit residuals with the new absorption coefficients (using the qSDV), as seen in Figure 5a. Absorption coefficients calculated with the qSDV were used to retrieve total columns of O_2 from solar spectra recorded over a one year period at TCCON sites in Eureka (eu) (Nunavut, Canada) (Batchelor et al., 2009), Park Falls (pa) (Wisconsin, U.S.A) (Washenfelder et al., 2006b), Lamont (oc) (Oklahoma, U.S.A), and Darwin (db) (Australia) (Deutscher et al., 2010). In total 131 124 spectra were fit using the qSDV and the average root mean square (RMS) residual of the fit only decreased by 0.5 %.

5. Impact of O_2 Columns on XCO_2 Measurements

The O_2 column retrieved from the $1.27\ \mu\text{m}$ band with a Voigt line shape and spectroscopic parameters from the atm.101 line list (Wunch, D. et al., 2015) has an airmass dependence such that the O_2 column retrieved increases as a function of solar zenith angle (or airmass). Using spectra recorded from Eureka, Park Falls, Lamont, and Darwin over one-year periods, total columns of O_2 were retrieved using (1) a Voigt spectral line shape with spectroscopic parameters from the atm.101 line list and (2) the qSDV with the spectroscopic parameters determined in Section 3. Figure 6 shows the percent difference calculated as the column from the qSDV retrieval minus the column from the Voigt retrieval, which was then divided by the latter and multiplied by 100, plotted as a function of solar zenith angle (SZA). At the smallest SZA, the qSDV retrieves 0.75% less O_2 than the Voigt, with the difference increasing to approximately 1.8% as the SZA approaches 90° .

5.1 Airmass Dependence of XCO_2

Since the standard TCCON XCO_2 (and all other $XGas$) is calculated using the column of O_2 instead of the surface pressure, errors associated with the retrieval of O_2 , such as the airmass dependence of the O_2 column, will affect XCO_2 . In order correct for this, an empirical correction is applied to all TCCON XCO_2 (and $XGas$). The empirical correction determines the antisymmetrical component of the day's XCO_2 , which is assumed to be the true variation of XCO_2 throughout the day, as well as the symmetrical component, which is caused by the airmass dependence of



the retrieved column of the gas of interest and O₂. We can, therefore, represent a measurement as (Wunch et al., 2011):

$$y_i = \hat{y}[1 + \alpha S(\theta_i) + \beta A(t_i)] \quad (5)$$

where \hat{y} is the mean value of XCO₂ measured that day, β is the fitted coefficient of the antisymmetric function $A(t_i)$ and α is the fitted coefficient of the symmetric function $S(\theta_i)$. The antisymmetric function is calculated by (Wunch et al., 2011):

$$A(t_i) = \sin(2\pi(t_i - t_{noon})) \quad (6)$$

where t_i is the time of the measurement and t_{noon} is the time at solar noon, both in units of days. The symmetric function is calculated by (Wunch et al., 2011):

$$S(\theta_i) = \left(\frac{\theta_i + 13^\circ}{90^\circ + 13^\circ} \right)^3 - \left(\frac{\theta_i - 13^\circ}{90^\circ - 13^\circ} \right)^3 \quad (7)$$

where θ_i is the SZA in degrees. To determine α for the different line shapes, total columns of CO₂ were retrieved using the Voigt line shape (Wunch, D. et al., 2015) and the qSDV with line mixing (Mendonca et al., 2016). Henceforth, we will refer to XCO₂ calculated from O₂ and CO₂ using the Voigt line shape as XCO₂ Voigt and the qSDV line shape as XCO₂ qSDV.

Figure 7 shows the average α calculated for each season at Darwin, Lamont, and Park Falls. Eureka XCO₂ cannot be used to determine α because Eureka measurements do not go through the same range of SZAs as the other three sites due to its geolocation. The average α XCO₂ Voigt are represented by stars in Figure 7, while the squares indicate XCO₂ qSDV. At all three sites, α is closer to 0 when the qSDV line shape is used in the retrieval compared to the Voigt retrieval, regardless of the season. The average α for XCO₂ Voigt calculated from a year of measurements from Darwin, Park Falls, and Lamont is -0.0071 ± 0.0057 and that for XCO₂ qSDV is -0.0012 ± 0.0054 .

For all four sites, $\alpha = -0.0071$ is used to correct XCO₂ Voigt measurements. Figure 8a shows the XCO₂ Voigt anomalies plotted as a function of SZA. The data is expressed as the daily XCO₂ anomaly, which is the difference between the XCO₂ value and the daily median value, in order to remove the seasonal cycle. When XCO₂ is left uncorrected for airmass, there is a clear airmass dependence where the amount of XCO₂ decreases as a function of SZA up to a SZA of approximately 82°, at which point XCO₂ increases as a function of SZA. Figure 8b shows XCO₂ Voigt corrected for the airmass dependence. This airmass correction works well up to a SZA of approximately 82°, after which the correction only serves to increase the airmass dependence. Figure 8c is the same as 8a but for the uncorrected XCO₂ qSDV measurements, while Figure 8d is the same as 8b but for the corrected XCO₂ qSDV measurements. When the airmass correction is applied to XCO₂ qSDV there is a small difference between the corrected and uncorrected XCO₂ qSDV measurements, with the difference only noticeable for the Darwin measurements recorded at SZA > 60°. For XCO₂ qSDV measurements made at SZA > 82° XCO₂ does not increase with SZA as it does with the Voigt.



258 5.2 Accuracy of XCO₂

259 To assess the accuracy of TCCON XCO₂ measurements, they are compared to aircraft XCO₂ profile measurements
 260 using the method described in Wunch et al. (2010). Figure 9a shows the comparison between the aircraft XCO₂
 261 measurements (legend on the top details the different aircraft) and TCCON XCO₂ Voigt measurements for 13
 262 TCCON sites (given by the color-coded legend on the bottom right). The gray line indicates the one-to-one line and
 263 the dashed line is the line of best fit. There is a bias of 0.9897 ± 0.0005 , as given by the slope of the line of best fit in
 264 Figure 9a, for the XCO₂ Voigt measurements. Figure 9b is the same as 9a but for the XCO₂ qSDV measurements.
 265 The bias between the aircraft XCO₂ measurements and the XCO₂ qSDV measurements is 1.0041 ± 0.0005 as given
 266 by the slope of the line of best fit in Figure 9b. Using the qSDV to retrieve total columns of CO₂ and O₂ thus reduces
 267 the difference between TCCON XCO₂ and aircraft XCO₂ measurements by 0.62 %.

268 TCCON XCO₂ measurements are divided by the scale factors (or bias determined in Figure 9) to calibrate to the
 269 WMO scale. For all TCCON XCO₂ measurements retrieved with a Voigt line shape, the airmass correction is first
 270 applied to the data and the result is divided by the determined bias factor, 0.9897. Figure 10a to 10d shows XCO₂
 271 Voigt (for Eureka, Park Falls, Lamont, and Darwin respectively) indicated by red square boxes in the plots. XCO₂
 272 Voigt measurements made at $\text{SZA} > 82^\circ$ have been filtered out because they cannot be corrected for the airmass
 273 dependence. The blue boxes are XCO₂ qSDV corrected for airmass dependence and scaled by 1.0041. No filter was
 274 applied to the XCO₂ qSDV measurements for SZA since the airmass dependence correction works at all SZA.
 275 Figure 10e to 10h shows the difference between XCO₂ Voigt and XCO₂ qSDV for Eureka, Park Falls, Lamont, and
 276 Darwin respectively. The mean differences for the data shown in Figures 10e to 10h are 0.113 ± 0.082 , -
 277 0.102 ± 0.223 , -0.132 ± 0.241 , and -0.059 ± 0.231 $\mu\text{mol/mol}$ for Eureka, Park Falls, Lamont, and Darwin respectively.
 278 The difference throughout the day at Park Falls, Lamont, and Darwin varies between -0.6 to 0.2 $\mu\text{mol/mol}$ and is
 279 SZA dependent.

280 Figure 11a shows XCO₂ Voigt corrected for the airmass dependence, as well as XCO₂ qSDV, uncorrected and
 281 corrected for the airmass dependence. These XCO₂ measurements were retrieved from Park Falls spectra recorded
 282 on June 18, 2013. For all three XCO₂ measurements, the amount of XCO₂ decreases throughout the day. Figure 11b
 283 shows the difference between the corrected Voigt XCO₂ and the uncorrected qSDV XCO₂, as well as the difference
 284 between the corrected Voigt XCO₂ and the corrected qSDV XCO₂. The difference between the Voigt and the qSDV
 285 (corrected and uncorrected) shows that at the start and end of the day, more XCO₂ is retrieved with the qSDV, while
 286 at midday less is retrieved with the qSDV. The range in the differences seen in Figure 10e to 10h varies with SZA
 287 throughout the day as shown in Figure 11b.

288 6. Conclusions

289 Using cavity ring-down spectra measured in the lab, we have shown that the Voigt line shape is insufficient to
 290 model the line shape of O₂ for the 1.27 μm band, consistent with the results of (Hartmann et al. (2013) and
 291 Lamouroux et al. (2014). By using the speed-dependent Voigt line shape when calculating the absorption
 292 coefficients, we were better able to reproduce the measured absorption coefficients than using the Voigt line shape.



293 However, some residual structure still remains as seen Figures 1 and 2. This is partly due to the blending of spectral
 294 lines and the inability to retrieve the spectroscopic parameters for weak O₂ transitions. Fitting low-pressure spectra
 295 would help with isolating spectral lines and decreasing the uncertainty on the retrieved spectroscopic parameters for
 296 the Q branch lines. The pressure dependence of the retrieved speed-dependent width parameter is an indication that
 297 Dicke narrowing needs to be taken into account, as shown by Bui et al. (2014) for CO₂. However, when dealing
 298 with both speed dependence and Dicke narrowing, a multispectrum fit needs to be used due to the correlation
 299 between the parameters (Bui et al., 2014). The temperature dependence of the Lorentz width coefficients of this
 300 band has never been measured before, which could have an impact on the airmass dependence of O₂. Combining
 301 high-pressure cavity-ring-down absorption coefficient measurements with those for low pressures and different
 302 temperatures as done in Devi et al. (2015 and 2016) for CH₄ in would lead to more accurate line shape parameters
 303 for O₂.

304 By taking speed dependence into account for both CO₂ and O₂, we were able to significantly decrease the airmass
 305 dependence of TCCON XCO₂ and the bias between TCCON and aircraft XCO₂. With the qSDV line shape, XCO₂
 306 measurements made at SZA > 82° no longer have to be discarded, resulting in more XCO₂ measurement available
 307 from all TCCON sites. This is particularly important for high-latitude TCCON sites, such as Eureka, because
 308 measurements made from late February to late March and from late September until mid-October are made at SZA
 309 > 82°. Filtering out these large SZA measurements thus limits the knowledge of the seasonal cycle of XCO₂ at high
 310 latitudes. The airmass dependence of the O₂ column not only effects XCO₂ but all trace gases measured by TCCON
 311 and in the future the airmass dependence of all XGas will be determined with these new O₂ columns.

312 Acknowledgements

313 This work was primarily supported by the Canadian Space Agency (CSA) through the GOSAT and CAFTON
 314 projects and the Natural Sciences and Engineering Research Council of Canada (NSERC). The Eureka
 315 measurements were made at the Polar Environment Atmospheric Research Laboratory (PEARL) by the Canadian
 316 Network for the Detection of Atmospheric Change (CANDAC), which has been supported by the AIF/NSRIT, CFI,
 317 CFCAS, CSA, Environment Canada (EC), Government of Canada IPY funding, NSERC, OIT, ORF, PCSP, and
 318 FQRNT. The authors wish to thank the staff at EC's Eureka Weather Station and CANDAC for the logistical and
 319 on-site support provided. Thanks to CANDAC Principal Investigator James R. Drummond, PEARL Site Manager
 320 Pierre Fogal, and CANDAC/PEARL operators Mike Maurice and Peter McGovern, for their invaluable assistance in
 321 maintaining and operating the Bruker 125HR. The research at the Jet Propulsion Laboratory (JPL), and California
 322 Institute of Technology was performed under contracts and cooperative agreements with the National Aeronautics
 323 and Space Administration (NASA). Geoff Toon and Debra Wunch acknowledge support from NASA for
 324 the development of TCCON via grant number NNX17AE15G. Darwin TCCON measurements are possible thanks
 325 to support from NASA grants NAG5-12247 and NNG05-GD07G, the Australian Research Council grants
 326 DP140101552, DP110103118, DP0879468 and LP0562346, and the DOE ARM program for technical support. The
 327 research at the National Institute of Standards and Technology was performed with the support of the NIST
 328 Greenhouse Gas Measurements and Climate Research Program. Certain commercial equipment, instruments, or



329 materials are identified in this paper in order to specify the experimental procedure adequately. Such identification is
330 not intended to imply recommendation or endorsement by the National Institute of Standards and Technology, nor is
331 it intended to imply that the materials or equipment identified are necessarily the best available for the purpose.

332

333

334

335

336

337

338

339

340

341

342

343

344

345

346

347

348

349

350

351

352

353

354

355

356

357

358 **References**

- 359 Abrarov, S.M., Quine, B.M., 2011. Efficient algorithmic implementation of the Voigt/complex error function based
360 on exponential series approximation. *Appl. Math. Comput.* 218, 1894–1902.
361 <https://doi.org/10.1016/j.amc.2011.06.072>
- 362 Batchelor, R.L., Strong, K., Lindenmaier, R., Mittermeier, R.L., Fast, H., Drummond, J.R., Fogal, P.F., 2009. A
363 New Bruker IFS 125HR FTIR Spectrometer for the Polar Environment Atmospheric Research Laboratory
364 at Eureka, Nunavut, Canada: Measurements and Comparison with the Existing Bomem DA8 Spectrometer.
365 *J. Atmospheric Ocean. Technol.* 26, 1328–1340. <https://doi.org/10.1175/2009JTECHA1215.1>
- 366 Bergland, G., 1969. A radix-eight fast Fourier transform subroutine for real-valued series. *IEEE Trans. Audio*
367 *Electroacoustics* 17, 138–144. <https://doi.org/10.1109/TAU.1969.1162043>
- 368 Bernath, P.F., McElroy, C.T., Abrams, M.C., Boone, C.D., Butler, M., Camy-Peyret, C., Carleer, M., Clerbaux, C.,
369 Coheur, P.-F., Colin, R., DeCola, P., DeMazière, M., Drummond, J.R., Dufour, D., Evans, W.F.J., Fast, H.,
370 Fussen, D., Gilbert, K., Jennings, D.E., Llewellyn, E.J., Lowe, R.P., Mahieu, E., McConnell, J.C.,
371 McHugh, M., McLeod, S.D., Michaud, R., Midwinter, C., Nassar, R., Nichitiu, F., Nowlan, C., Rinsland,
372 C.P., Rochon, Y.J., Rowlands, N., Semeniuk, K., Simon, P., Skelton, R., Sloan, J.J., Soucy, M.-A., Strong,
373 K., Tremblay, P., Turnbull, D., Walker, K.A., Walkty, I., Wardle, D.A., Wehrle, V., Zander, R., Zou, J.,
374 2005. Atmospheric Chemistry Experiment (ACE): Mission overview. *Geophys. Res. Lett.* 32, L15S01.
375 <https://doi.org/10.1029/2005GL022386>
- 376 Bui, T.Q., Long, D.A., Cygan, A., Sironneau, V.T., Hogan, D.W., Rupasinghe, P.M., Ciurylo, R., Lisak, D.,
377 Okumura, M., 2014. Observations of Dicke narrowing and speed dependence in air-broadened CO₂
378 lineshapes near 2.06 μm . *J. Chem. Phys.* 141, 174301. <https://doi.org/10.1063/1.4900502>
- 379 Cheah, S.-L., Lee, Y.-P., Ogilvie, J.F., 2000. Wavenumbers, strengths, widths and shifts with pressure of lines in
380 four bands of gaseous ¹⁶O₂ in the systems a¹ Δ_g -X³ Σ_g^- and b¹ Σ_g^+ -X³ Σ_g^- . *J. Quant. Spectrosc. Radiat. Transf.*
381 64, 467–482. [https://doi.org/10.1016/S0022-4073\(99\)00126-0](https://doi.org/10.1016/S0022-4073(99)00126-0)
- 382 Ciurylo, R., 1998. Shapes of pressure- and Doppler-broadened spectral lines in the core and near wings. *Phys. Rev.*
383 *A* 58, 1029–1039. <https://doi.org/10.1103/PhysRevA.58.1029>
- 384 Crisp, D., Atlas, R.M., Breon, F.-M., Brown, L.R., Burrows, J.P., Ciais, P., Connor, B.J., Doney, S.C., Fung, I.Y.,
385 Jacob, D.J., Miller, C.E., O'Brien, D., Pawson, S., Randerson, J.T., Rayner, P., Salawitch, R.J., Sander,
386 S.P., Sen, B., Stephens, G.L., Tans, P.P., Toon, G.C., Wennberg, P.O., Wofsy, S.C., Yung, Y.L., Kuang, Z.,
387 Chudasama, B., Sprague, G., Weiss, B., Pollock, R., Kenyon, D., Schroll, S., 2004. The Orbiting Carbon
388 Observatory (OCO) mission. *Adv. Space Res., Trace Constituents in the Troposphere and Lower*
389 *Stratosphere* 34, 700–709. <https://doi.org/10.1016/j.asr.2003.08.062>
- 390 Deutscher, N.M., Griffith, D.W.T., Bryant, G.W., Wennberg, P.O., Toon, G.C., Washenfelder, R.A., Keppel-Aleks,
391 G., Wunch, D., Yavin, Y., Allen, N.T., Blavier, J.-F., Jiménez, R., Daube, B.C., Bright, A.V., Matross,
392 D.M., Wofsy, S.C., Park, S., 2010. Total column CO₂ measurements at Darwin, Australia – site description
393 and calibration against in situ aircraft profiles. *Atmos Meas Tech* 3, 947–958. [https://doi.org/10.5194/amt-](https://doi.org/10.5194/amt-3-947-2010)
394 [3-947-2010](https://doi.org/10.5194/amt-3-947-2010)
- 395 Devi, V.M., Benner, D.C., Sung, K., Brown, L.R., Crawford, T.J., Yu, S., Smith, M.A.H., Mantz, A.W., Boudon,
396 V., Ismail, S., 2016. Spectral line parameters including line shapes in the 2v₃ Q branch of ¹²CH₄. *J. Quant.*
397 *Spectrosc. Radiat. Transf., XVIIIth Symposium on High Resolution Molecular Spectroscopy (HighRus-*
398 *2015), Tomsk, Russia* 177, 152–169. <https://doi.org/10.1016/j.jqsrt.2015.12.009>
- 399 Devi, V.M., Benner, D.C., Sung, K., Crawford, T.J., Yu, S., Brown, L.R., Smith, M.A.H., Mantz, A.W., Boudon,
400 V., Ismail, S., 2015. Self- and air-broadened line shapes in the 2v₃ P and R branches of ¹²CH₄. *J. Mol.*
401 *Spectrosc., Spectroscopy with Synchrotron Radiation* 315, 114–136.
402 <https://doi.org/10.1016/j.jms.2015.05.003>
- 403 Gordon, I.E., Kass, S., Campargue, A., Toon, G.C., 2010. First identification of the electric quadrupole transitions
404 of oxygen in solar and laboratory spectra. *J. Quant. Spectrosc. Radiat. Transf., Special Issue Dedicated to*
405 *Laurence S. Rothman on the Occasion of his 70th Birthday.* 111, 1174–1183.
406 <https://doi.org/10.1016/j.jqsrt.2010.01.008>
- 407 Hartmann, J.-M., Sironneau, V., Boulet, C., Svensson, T., Hodges, J.T., Xu, C.T., 2013. Collisional broadening and
408 spectral shapes of absorption lines of free and nanopore-confined O₂ gas. *Phys. Rev. A* 87, 032510.
409 <https://doi.org/10.1103/PhysRevA.87.032510>
- 410 Hodges, J.T., 2005. Automated high-resolution frequency-stabilized cavity ring-down absorption spectrometer. *Rev.*
411 *Sci. Instrum.* 76, 023112. <https://doi.org/10.1063/1.1850633>



- Hodges, J.T., Layer, H.P., Miller, W., Scace, G.E., 2004. Frequency-stabilized single-mode cavity ring-down apparatus for high-resolution absorption spectroscopy. *Rev. Sci. Instrum.* 75, 849–863. <https://doi.org/10.1063/1.1666984>
- Keppel-Aleks, G., Toon, G.C., Wennberg, P.O., Deutscher, N.M., 2007. Reducing the impact of source brightness fluctuations on spectra obtained by Fourier-transform spectrometry. *Appl. Opt.* 46, 4774. <https://doi.org/10.1364/AO.46.004774>
- Lamoureux, J., Sironneau, V., Hodges, J.T., Hartmann, J.-M., 2014. Isolated line shapes of molecular oxygen: Requanted classical molecular dynamics calculations versus measurements. *Phys. Rev. A* 89, 042504. <https://doi.org/10.1103/PhysRevA.89.042504>
- Leshchishina, O., Kass, S., Gordon, I.E., Rothman, L.S., Wang, L., Campargue, A., 2010. High sensitivity CRDS of the $a^1\Delta_g-X^3\Sigma_g^-$ band of oxygen near 1.27 μm : Extended observations, quadrupole transitions, hot bands and minor isotopologues. *J. Quant. Spectrosc. Radiat. Transf.*, XVIth Symposium on High Resolution Molecular Spectroscopy (HighRus-2009) XVIth Symposium on High Resolution Molecular Spectroscopy 111, 2236–2245. <https://doi.org/10.1016/j.jqsrt.2010.05.014>
- Leshchishina, O., Kass, S., Gordon, I.E., Yu, S., Campargue, A., 2011. The band of $^{16}\text{O}^{17}\text{O}$, $^{17}\text{O}^{18}\text{O}$ and $^{17}\text{O}_2$ by high sensitivity CRDS near 1.27 μm . *J. Quant. Spectrosc. Radiat. Transf.* 112, 1257–1265. <https://doi.org/10.1016/j.jqsrt.2011.01.014>
- Lin, H., Reed, Z.D., Sironneau, V.T., Hodges, J.T., 2015. Cavity ring-down spectrometer for high-fidelity molecular absorption measurements. *J. Quant. Spectrosc. Radiat. Transf.* 161, 11–20. <https://doi.org/10.1016/j.jqsrt.2015.03.026>
- Long, D.A., Havey, D.K., Okumura, M., Miller, C.E., Hodges, J.T., 2010. O₂ A-band line parameters to support atmospheric remote sensing. *J. Quant. Spectrosc. Radiat. Transf.* 111, 2021–2036. <https://doi.org/10.1016/j.jqsrt.2010.05.011>
- Maté, B., Lugez, C., Fraser, G.T., Lafferty, W.J., 1999. Absolute intensities for the O₂ 1.27 μm continuum absorption. *J. Geophys. Res. Atmospheres* 104, 30585–30590. <https://doi.org/10.1029/1999JD900824>
- Mendonça, J., Strong, K., Toon, G.C., Wunch, D., Sung, K., Deutscher, N.M., Griffith, D.W.T., Franklin, J.E., 2016. Improving atmospheric CO₂ retrievals using line mixing and speed-dependence when fitting high-resolution ground-based solar spectra. *J. Mol. Spectrosc., Atmospheric Spectroscopy* 323, 15–27. <https://doi.org/10.1016/j.jms.2016.01.007>
- Mertz, L., 1967. Auxiliary computation for Fourier spectrometry. *Infrared Phys.* 7, 17–23. [https://doi.org/10.1016/0020-0891\(67\)90026-7](https://doi.org/10.1016/0020-0891(67)90026-7)
- Mlawer, E.J., Clough, S.A., Brown, P.D., Stephen, T.M., Landry, J.C., Goldman, A., Murcray, F.J., 1998. Observed atmospheric collision-induced absorption in near-infrared oxygen bands. *J. Geophys. Res. Atmospheres* 103, 3859–3863. <https://doi.org/10.1029/97JD03141>
- Newman, S.M., Lane, I.C., Orr-Ewing, A.J., Newnham, D.A., Ballard, J., 1999. Integrated absorption intensity and Einstein coefficients for the O₂ $a^1\Delta_g-X^3\Sigma_g^-$ (0,0) transition: A comparison of cavity ringdown and high resolution Fourier transform spectroscopy with a long-path absorption cell. *J. Chem. Phys.* 110, 10749–10757. <https://doi.org/10.1063/1.479018>
- Newman, S.M., Orr-Ewing, A.J., Newnham, D.A., Ballard, J., 2000. Temperature and pressure dependence of line widths and integrated absorption intensities for the O₂ $a^1\Delta_g-X^3\Sigma_g^-$ (0,0) transition. *J. Phys. Chem. A* 104, 9467–9480.
- Ngo, N.H., Lisak, D., Tran, H., Hartmann, J.-M., 2013. An isolated line-shape model to go beyond the Voigt profile in spectroscopic databases and radiative transfer codes. *J. Quant. Spectrosc. Radiat. Transf.* 129, 89–100. <https://doi.org/10.1016/j.jqsrt.2013.05.034>
- Predoi-Cross, A., Hambrook, K., Keller, R., Povey, C., Schofield, I., Hurtmans, D., Over, H., Mellau, G.C., 2008. Spectroscopic lineshape study of the self-perturbed oxygen A-band. *J. Mol. Spectrosc.* 248, 85–110. <https://doi.org/10.1016/j.jms.2007.11.007>
- Rohart, F., Mäder, H., Nicolaisen, H.-W., 1994. Speed dependence of rotational relaxation induced by foreign gas collisions: Studies on CH₃F by millimeter wave coherent transients. *J. Chem. Phys.* 101, 6475–6486. <https://doi.org/10.1063/1.468342>
- Rothman, L.S., Gordon, I.E., Babikov, Y., Barbe, A., Chris Benner, D., Bernath, P.F., Birk, M., Bizzocchi, L., Boudon, V., Brown, L.R., Campargue, A., Chance, K., Cohen, E.A., Coudert, L.H., Devi, V.M., Drouin, B.J., Fayt, A., Flaud, J.-M., Gamache, R.R., Harrison, J.J., Hartmann, J.-M., Hill, C., Hodges, J.T., Jacquemart, D., Jolly, A., Lamoureux, J., Le Roy, R.J., Li, G., Long, D.A., Lyulin, O.M., Mackie, C.J., Massie, S.T., Mikhailenko, S., Müller, H.S.P., Naumenko, O.V., Nikitin, A.V., Orphal, J., Perevalov, V., Perrin, A., Polovtseva, E.R., Richard, C., Smith, M.A.H., Starikova, E., Sung, K., Tashkun, S., Tennyson,



- 468 J., Toon, G.C., Tyuterev, V.G., Wagner, G., 2013a. The HITRAN2012 molecular spectroscopic database. *J.*
469 *Quant. Spectrosc. Radiat. Transf.*, HITRAN2012 special issue 130, 4–50.
470 <https://doi.org/10.1016/j.jqsrt.2013.07.002>
- 471 Rothman, L.S., Gordon, I.E., Barbe, A., Benner, D.C., Bernath, P.F., Birk, M., Boudon, V., Brown, L.R.,
472 Campargue, A., Champion, J.-P., Chance, K., Coudert, L.H., Dana, V., Devi, V.M., Fally, S., Flaud, J.-M.,
473 Gamache, R.R., Goldman, A., Jacquemart, D., Kleiner, I., Lacome, N., Lafferty, W.J., Mandin, J.-Y.,
474 Massie, S.T., Mikhailenko, S.N., Miller, C.E., Moazzen-Ahmadi, N., Naumenko, O.V., Nikitin, A.V.,
475 Orphal, J., Perevalov, V.I., Perrin, A., Predoi-Cross, A., Rinsland, C.P., Rotger, M., Šimečková, M., Smith,
476 M.A.H., Sung, K., Tashkun, S.A., Tennyson, J., Toth, R.A., Vandaele, A.C., Vander Auwera, J., 2009. The
477 HITRAN 2008 molecular spectroscopic database. *J. Quant. Spectrosc. Radiat. Transf.*, HITRAN 110, 533–
478 572. <https://doi.org/10.1016/j.jqsrt.2009.02.013>
- 479 Rothman, L.S., Jacquemart, D., Barbe, A., Chris Benner, D., Birk, M., Brown, L.R., Carleer, M.R., Chackerian Jr.,
480 C., Chance, K., Coudert, L.H., Dana, V., Devi, V.M., Flaud, J.-M., Gamache, R.R., Goldman, A.,
481 Hartmann, J.-M., Jucks, K.W., Maki, A.G., Mandin, J.-Y., Massie, S.T., Orphal, J., Perrin, A., Rinsland,
482 C.P., Smith, M.A.H., Tennyson, J., Tolchenov, R.N., Toth, R.A., Vander Auwera, J., Varanasi, P., Wagner,
483 G., 2005. The HITRAN 2004 molecular spectroscopic database. *J. Quant. Spectrosc. Radiat. Transf.* 96,
484 139–204. <https://doi.org/10.1016/j.jqsrt.2004.10.008>
- 485 Smith, K.M., Newnham, D.A., 2000. Near-infrared absorption cross sections and integrated absorption intensities of
486 molecular oxygen (O_2 , O_2-O_2 , and O_2-N_2). *J. Geophys. Res. Atmospheres* 105, 7383–7396.
487 <https://doi.org/10.1029/1999JD901171>
- 488 Smith, K.M., Newnham, D.A., Williams, R.G., 2001. Collision-induced absorption of solar radiation in the
489 atmosphere by molecular oxygen at 1.27 μm : Field observations and model calculations. *J. Geophys. Res.*
490 *Atmospheres* 106, 7541–7552. <https://doi.org/10.1029/2000JD900699>
- 491 Toon, G.C., 1991. The JPL MkIV interferometer. *Opt. Photonics News* 2, 19–21.
492 <https://doi.org/10.1364/OPN.2.10.000019>
- 493 Tran, H., Boulet, C., Hartmann, J.-M., 2006. Line mixing and collision-induced absorption by oxygen in the A band:
494 Laboratory measurements, model, and tools for atmospheric spectra computations. *J. Geophys. Res.*
495 *Atmospheres* 111, D15210. <https://doi.org/10.1029/2005JD006869>
- 496 Tran, H., Hartmann, J.-M., 2008. An improved O_2 A band absorption model and its consequences for retrievals of
497 photon paths and surface pressures. *J. Geophys. Res. Atmospheres* 113, D18104.
498 <https://doi.org/10.1029/2008JD010011>
- 499 Tran, H., Ngo, N.H., Hartmann, J.-M., 2013. Efficient computation of some speed-dependent isolated line profiles.
500 *J. Quant. Spectrosc. Radiat. Transf.* 129, 199–203. <https://doi.org/10.1016/j.jqsrt.2013.06.015>
- 501 Washenfelder, R.A., Toon, G.C., Blavier, J.-F., Yang, Z., Allen, N.T., Wennberg, P.O., Vay, S.A., Matross, D.M.,
502 Daube, B.C., 2006. Carbon dioxide column abundances at the Wisconsin Tall Tower site. *J. Geophys. Res.*
503 *Atmospheres* 111, D22305. <https://doi.org/10.1029/2006JD007154>
- 504 Wehr, R.A., 2005. Dicke -narrowed spectral lines in carbon monoxide buffered by argon (Ph.D.). University of
505 Toronto (Canada), Canada.
- 506 Wunch, D., Toon, G.C., Blavier, J.-F.L., Washenfelder, R.A., Notholt, J., Connor, B.J., Griffith, D.W.T., Sherlock,
507 V., Wennberg, P.O., 2011. The Total Carbon Column Observing Network. *Philos. Trans. R. Soc. Math.*
508 *Phys. Eng. Sci.* 369, 2087–2112. <https://doi.org/10.1098/rsta.2010.0240>
- 509 Wunch, D., Toon, G.C., Sherlock, V., Deutscher, N.M., Liu, C., Feist, D.G., Wennberg, P.O., 2015. The Total
510 Carbon Column Observing Network's GGG2014 Data Version.
511 <https://doi.org/10.14291/tcon.ggg2014.documentation.R0/1221662>
- 512 Wunch, D., Toon, G.C., Wennberg, P.O., Wofsy, S.C., Stephens, B.B., Fischer, M.L., Uchino, O., Abshire, J.B.,
513 Bernath, P., Biraud, S.C., Blavier, J.-F.L., Boone, C., Bowman, K.P., Browell, E.V., Campos, T., Connor,
514 B.J., Daube, B.C., Deutscher, N.M., Diao, M., Elkins, J.W., Gerbig, C., Gottlieb, E., Griffith, D.W.T.,
515 Hurst, D.F., Jiménez, R., Keppel-Aleks, G., Kort, E.A., Macatangay, R., Machida, T., Matsueda, H.,
516 Moore, F., Morino, I., Park, S., Robinson, J., Roehl, C.M., Sawa, Y., Sherlock, V., Sweeney, C., Tanaka,
517 T., Zondlo, M.A., 2010. Calibration of the Total Carbon Column Observing Network using aircraft profile
518 data. *Atmos Meas Tech* 3, 1351–1362. <https://doi.org/10.5194/amt-3-1351-2010>
- 519 Yokota, T., Yoshida, Y., Eguchi, N., Ota, Y., Tanaka, T., Watanabe, H., Maksyutov, S., 2009. Global
520 Concentrations of CO_2 and CH_4 Retrieved from GOSAT: First Preliminary Results. *Sola* 5, 160–163.
521 <https://doi.org/10.2151/sola.2009-041>
- 522



Figures

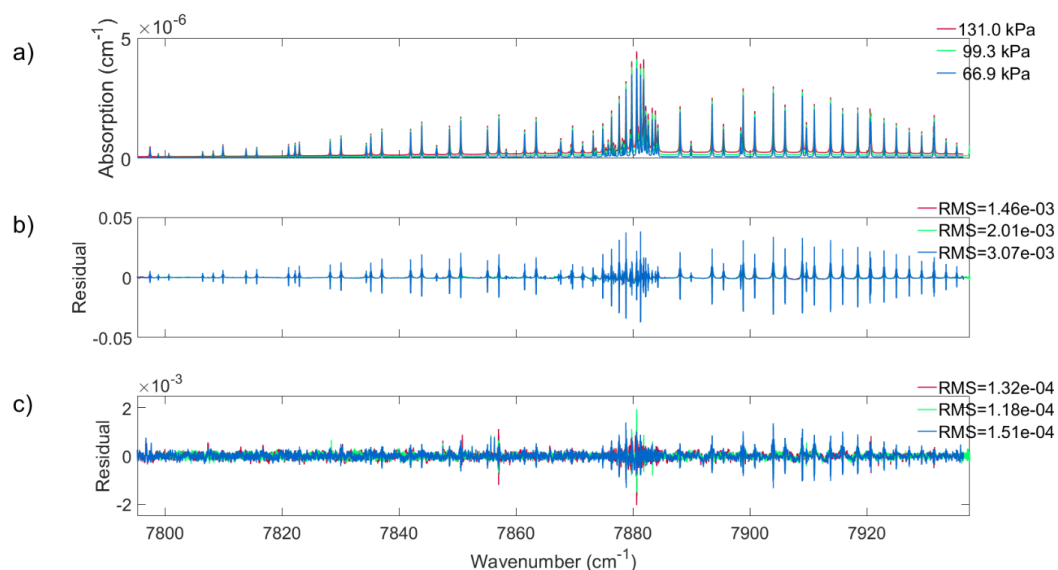


Figure 1: (a) Cavity-ring-down absorption coefficients measured at three pressures indicated in the legend at approximately room temperature and a volume mixing ratio of 0.20720(43) for O_2 . The difference between measured absorption coefficients and those calculated using (b) a Voigt line shape and (c) the speed dependent Voigt line shape. Note the difference in scale between panels (b) and (c).

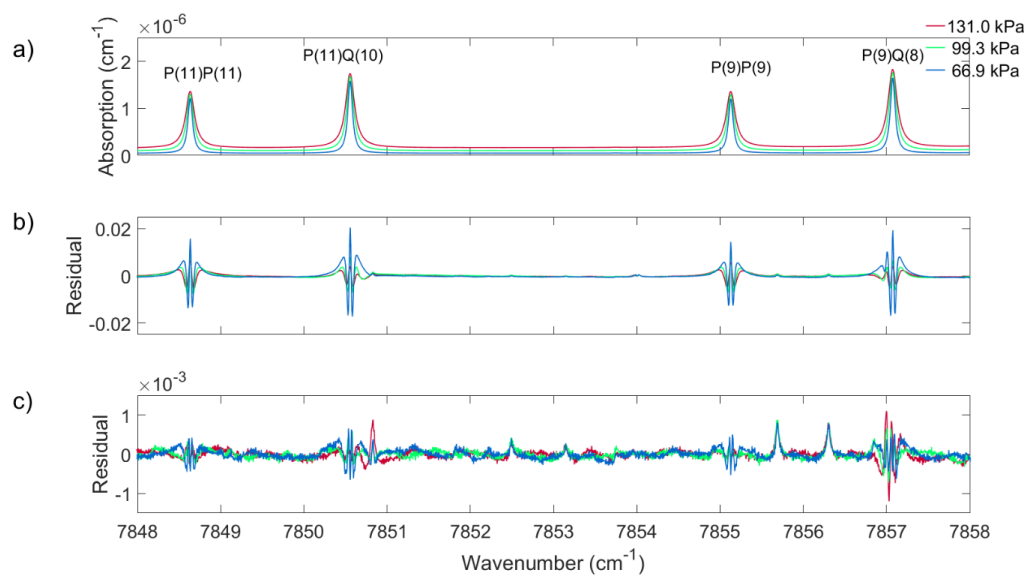


Figure 2: The same as Figure 1 but zoomed into four spectral lines in the P branch of the O₂ 1.27 μm band.

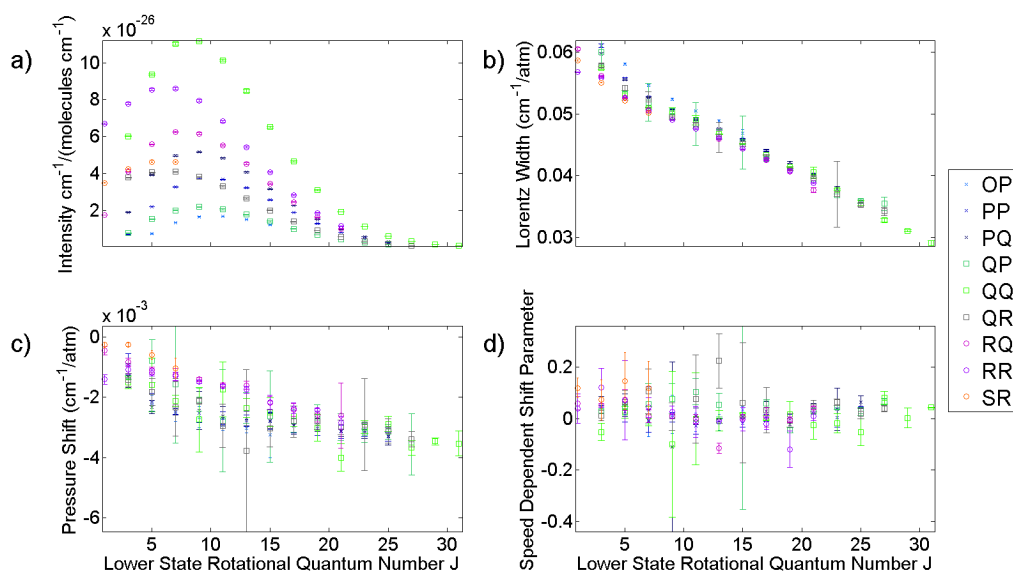


Figure 3: The averaged measured (a) intensity, (b) Lorentz, (c) pressure shift, and (d) speed-dependent pressure shift retrieved from the three cavity ring-down spectra. All data are plotted as a function of lower state rotational quantum number J and the uncertainties shown are 2σ .

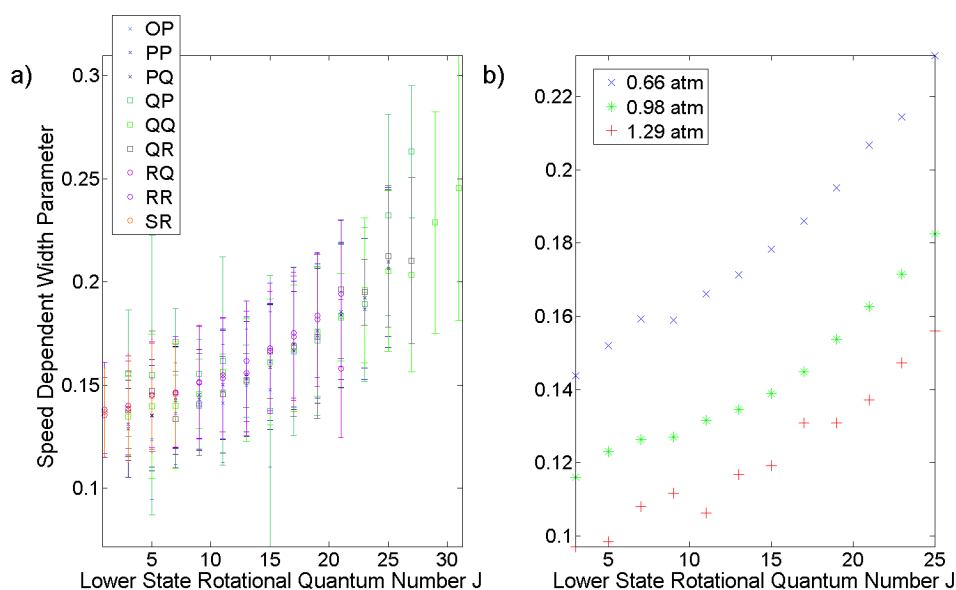


Figure 4: (a) The averaged measured speed-dependent width parameter plotted as a function of lower state rotational quantum number J'' . (b) The measured speed-dependent width parameter for spectral lines that belong to the PQ sub-branch plotted as a function of lower state rotational quantum number J'' .

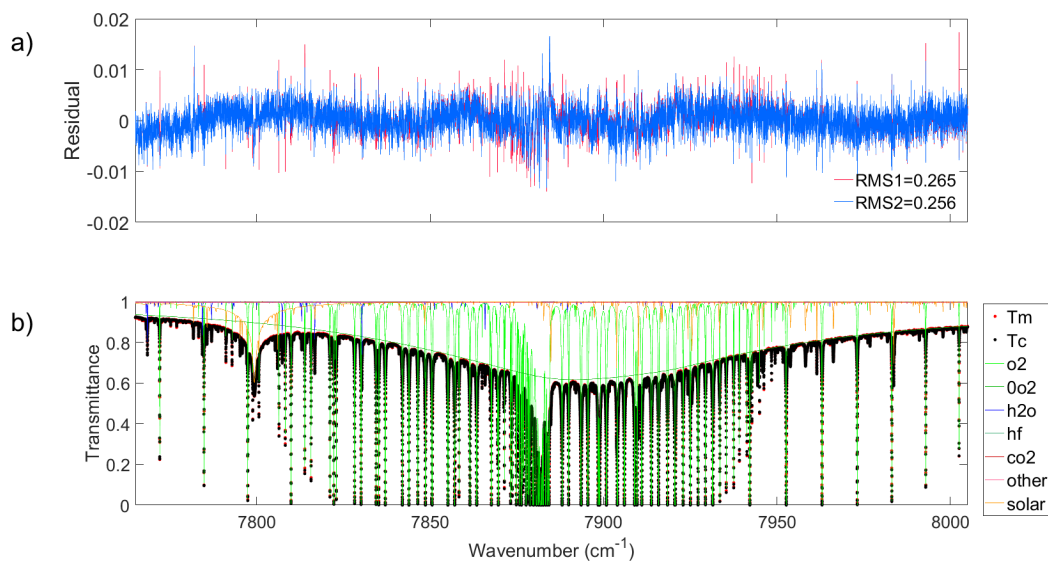
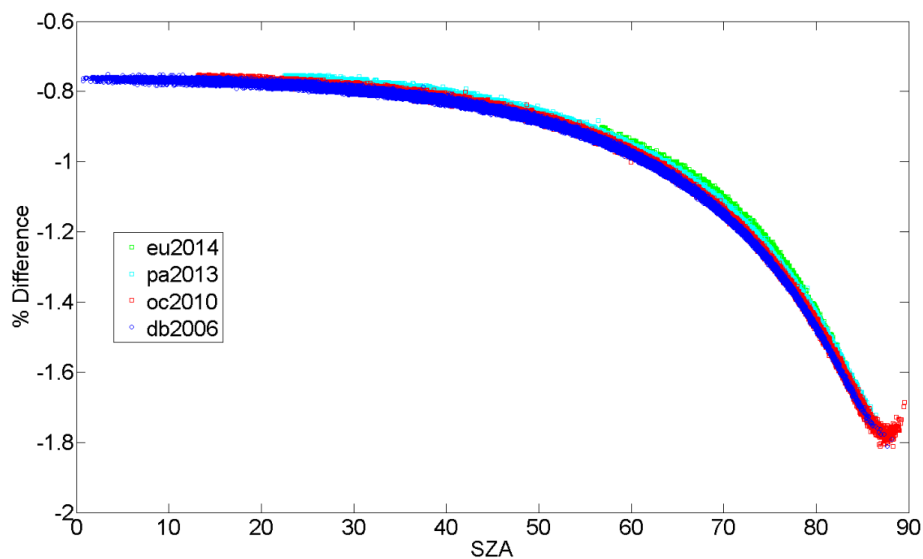


Figure 5: (a) The residuals (measured minus calculated) for a spectrum measured at Eureka on March 27, 2015 at a SZA of 81.32°. The red residual is the result of using the Voigt line shape and the blue is from using the qSDV. (b) The measured (red dots) and calculated (black dots), with the qSDV, spectrum, along with the gases included in the fit (refer to the legend to the right) in the spectral window.



572

573 **Figure 6: The percent difference between the O₂ column retrieved with the Voigt and qSDV line shapes for a**
 574 **year of measurements from Eureka (eu), Park Falls (pa), Lamont (oc), and Darwin (db).**

575

576

577

578

579

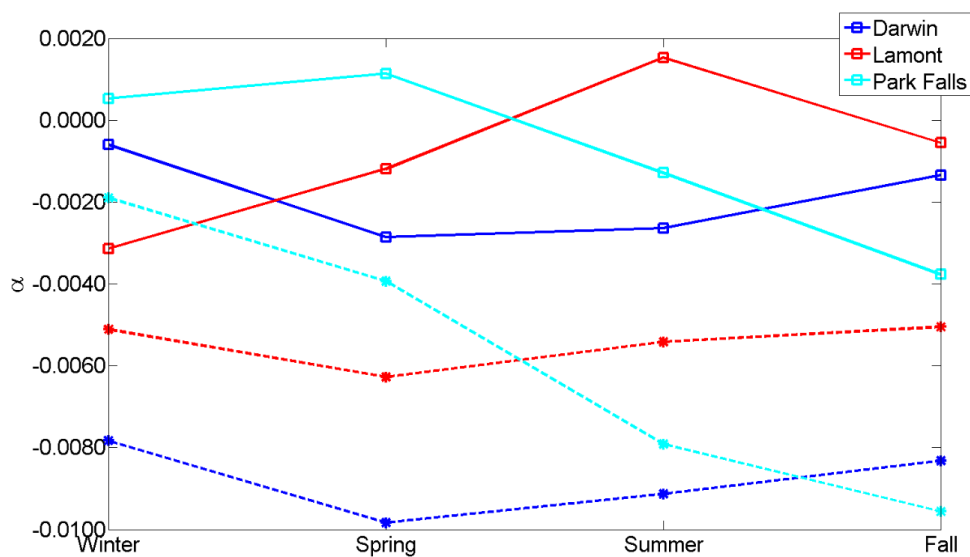


Figure 7: The average air mass-dependent correction factor for XCO₂ derived from a year of spectra measured at Darwin, Lamont, and Park Falls for different seasons. The dashed lines with stars are the α for XCO₂ retrieved using a Voigt line shape for both CO₂ and O₂ columns. The solid lines with squares are from XCO₂ retrieved using the qSDV for both CO₂ and O₂ columns.

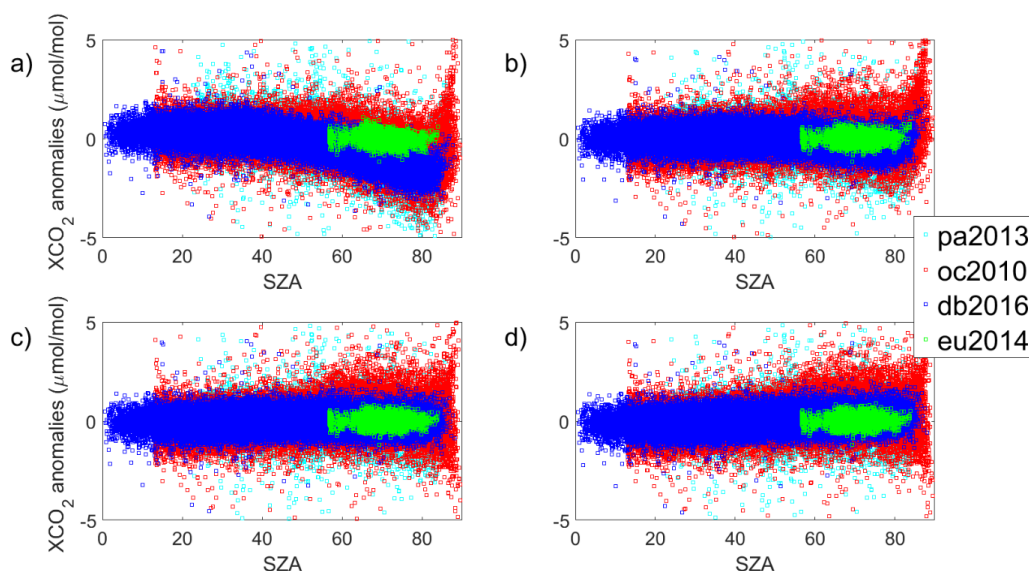


Figure 8: (a) XCO₂ Voigt anomaly for a year of measurements from the four TCCON sites. The XCO₂ anomaly is the difference between each XCO₂ value and the daily median XCO₂. (b) The XCO₂ Voigt anomaly after the airmass dependence correction is applied to the XCO₂ Voigt data. (c) XCO₂ qSDV anomaly. (d) XCO₂ qSDV anomaly after correction for the airmass dependence.

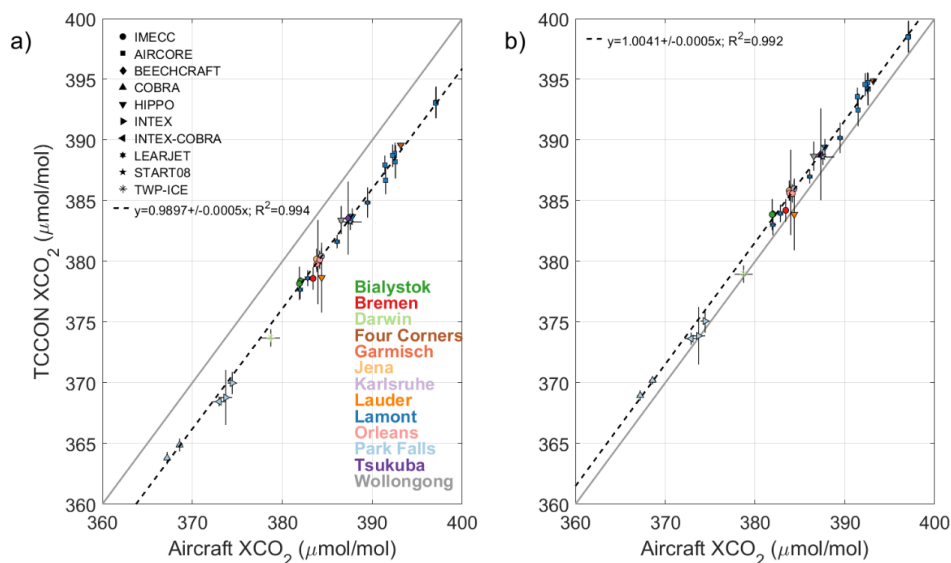
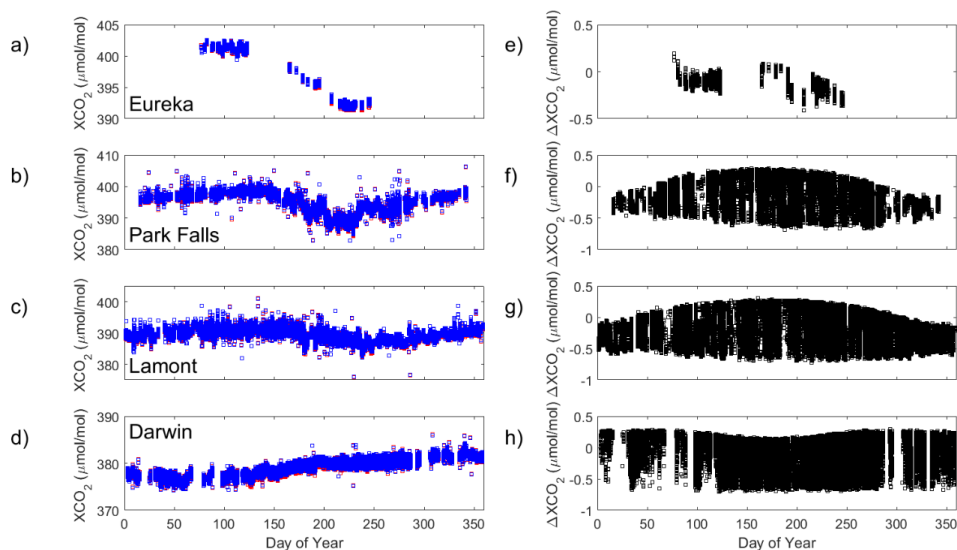


Figure 9: (a) Correlation between TCCON and aircraft XCO₂ Voigt measurements for 13 TCCON sites. Each aircraft type is indicated by a different symbol given by the legend in the top left corner. Each site is represented by a different colour given by the legend in the bottom right corner. The grey line indicates the one-to-one line and the dashed line is the line of best fit for the data. The slope of the line of best fit as well as the error on the slope are given in the plot. (b) the same as (a) but for XCO₂ qSDV.



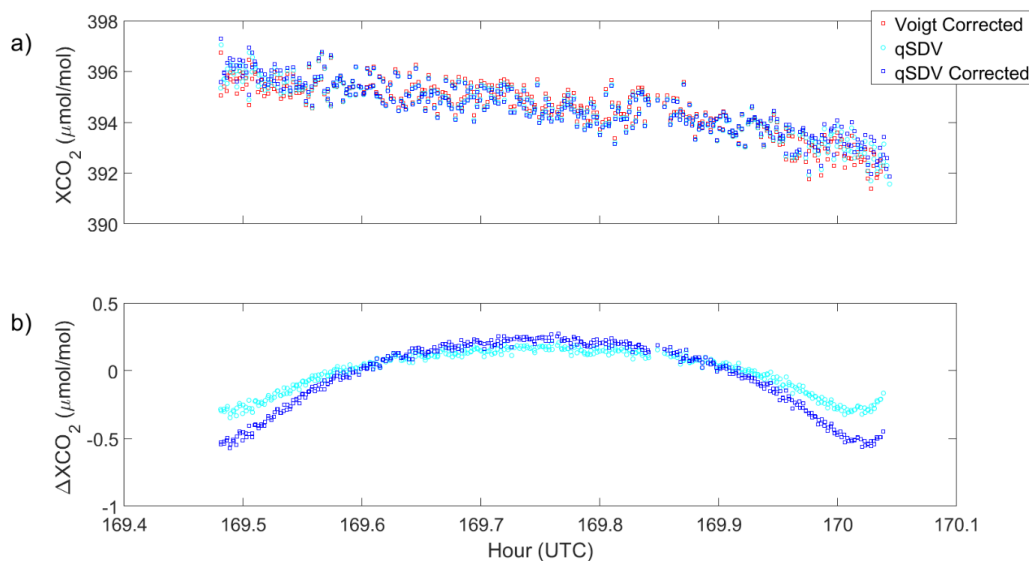
612

613 **Figure 10: (a) to (d) XCO₂ plotted as a function of day of the year for Eureka (2014), Park Falls (2013),**
 614 **Lamont (2010), and Darwin (2006) respectively. The red boxes are XCO₂ calculated from using a Voigt line**
 615 **shape in the retrieval and the blue boxes are from using the qSDV. (e) to (h) the difference between XCO₂**
 616 **Voigt and XCO₂ qSDV.**

617

618

619



620

621 **Figure 11: (a) XCO₂ from Park Falls retrieved from spectra recorded on June 18, 2013. Plotted is XCO₂**
 622 **retrieved: (1) with a Voigt line shape and corrected for the airmass dependence (red squares), (2) with the**
 623 **qSDV (cyan circles), and (3) with the qSDV and corrected for the airmass dependence (blue squares). (b) the**
 624 **difference between the Voigt XCO₂ corrected and the qSDV XCO₂ (cyan circles), and the difference between**
 625 **the Voigt XCO₂ corrected and the qSDV XCO₂ corrected (blue squares).**

626